Check for updates

Late-Quaternary paleoearthquakes along the Liulengshan Fault on the northern Shanxi Rift system

Wen Sun[1,2,3], Honglin He[1,2], Feng Shi[1,2]*, Zhanyu Wei[1,2], Haoyue Sun[1,2] and Peng Su[1,2]

[1]State Key Laboratory of Earthquake Dynamics, Institute of Geology, China Earthquake Administration, Beijing, China, [2]Shanxi Taiyuan Continental Rift Dynamics National Observation and Research Station, Beijing, China, [3]China Railway Engineering Design and Consulting Group Co., Ltd., Beijing, China

The Liulengshan Fault (LLSF), which lies on the northeastern edge of the Ordos Plateau, is a controlling boundary fault in the northern part of the Shanxi Rift system (SRS). The displaced landforms show that the fault has undergone strong and frequent late-Quaternary seismic activities. In 1989 and 1991, two moderate–strong earthquake swarms (Ms=6.1 and Ms=5.8) successively occurred in the LLSF, and GPS velocity shows that the areas are extending at around 1–2 mm/a. However, there is no surface-rupturing earthquake reported on the LLSF in historical records. Thus, the study of paleoseismic history and rupture behavior of paleoearthquakes in late-Quaternary on the LLSF is of fundamental importance for understanding the future seismic risk of this fault. To solve these problems, we conducted paleoseismological trench excavations at two sites on the LLSF to establish its paleoearthquake history. On the basis of the field geological survey and interpretation of high-precision topographic data, we carried out large-scale fault mapping and excavated two trenches in Xujiabao and Luofengwa across the LLSF. Then, four events in the Xujiabao trench and three events in the Luofengwa trench are identified. Finally, combined with radiocarbon dating (C14), optically stimulated luminescence (OSL) and OxCal modeling, we constrained the ages of these events. Together with the previous results of paleoseismology in Yin et al. (1997), we consider that different segments of the LLSF may rupture together at the same time. Therefore, a total of six paleoearthquake events since late-Quaternary have been finally confirmed at 44,151−30881a, 40,163-28045a, 28,233-19215a, 16,742-12915a, 12,788-8252a, and 8203−2300a BP. According to the empirical relationships between moment magnitude and rupture length, the best estimated magnitude is inferred to be in the range between Mw 6.9 and Mw 7.7. Considering the strong late-Quaternary activity and a long earthquake elapsed time, we propose that the LLSF might have a high seismic hazard potential in the near future.

Introduction

The Shanxi Rift system (SRS) of northern China is wellknown for its intense neo-tectonics and strong earthquakes (Molnar and Tapponnier, 1977; Northrup et al., 1995; Ren et al., 2002). The main boundary faults of the SRS are active, and in the past thousand years, a number of destructive earthquakes (M≥7) occurred along these faults (Lee et al., 1978; Liu et al., 2004; Deng et al., 2007; Rao et al., 2018; Xu et al., 2018) (Figure 1). Previous studies in the northern Shanxi Grabens, at the northeastern corner of the Ordos Plateau in northern China, have found extension rates of anywhere between 0 and 6 mm

a−1 at an azimuth between 95° and 180° (Zhang et al., 1998; Shen et al., 2000; Wang et al., 2011; Wang et al., 2012; Zhang et al., 2018). On the basis of Quaternary, seismic, and geodetic rates of strain, Middleton et al. (2017) conclude that the northern Shanxi Grabens are extending at around 1–2 mm/a at an azimuth of ≈151°.

Contrastingly, there is no historical record of large-magnitude earthquakes (M≥7) in the northern Shanxi Rift system (Datong Graben) (Figure 1) (Wesnousky et al., 1984; China Earthquake Administration, 1999a; Liu et al.,2007). Determining whether large-magnitude earthquakes can occur in the northern Shanxi Rift system is very important for

FIGURE 1
Shuttle Radar Topography Mission (SRTM) topography of the Shanxi Rift system in North China. The red lines and red circles represent major active faults and major historical earthquakes with magnitudes greater than M7, respectively (Working Group on Historical Earthquake Compilation of Shanxi Province Earthquake Administration, 1991). Horizontal GPS (global position system) velocities relative to the stable Eurasian plate (Wang and Shen, 2020), focal mechanisms of instrumental earthquakes with Mw > 5 (CMT catalog, Ekström et al., 2012). Inset globe shows the location of Figure 1 with Asia. Major faulted basins and faults: WHB, Weihe Basin; YCB, Yuncheng Basin; LFB, Linfen Basin; TYB, Taiyuan Basin; XDB, Xinding Basin; DTB, Datong Basin; HSPF, Huashan Piedmont Fault; ZTSF, Zhongtiaoshan Fault; LYSF, Luoyunshan Fault; HPF, Huoshan Piedmont Fault; JCF, Jiaocheng Fault; TGF, Taigu Fault; XZF, Xizhoushan Fault; WTF: Wutaishan Fault; HSNF: Hengshan Northern Fault; YGF, Yangyuan Graben Fault; KQF, Kouquan Fault; DQSF, Daqingshan Fault; and LLSF, Liulengshan Fault.

TABLE 1 Unit descriptions from the exposed walls of the Xujiabao trench.

Unit no.	Description
U1	Sequence of earthy pebbly fine sand-silt layer with several brown gravel beds, with clear stratification. This unit can be further divided into many subunits, but there is no obvious layer opposite to it in the hanging side. The gravel diameter in gravel beds is generally 3–5 cm, and the psephicity is normal
U2	The unit consists of two subunits, u2-1 and u2-2, with a gravel layer at the top and a silt layer containing fine gravel at the bottom
U3	u3-1, u3-2, and u3-3 of the main fault's hanging side are composed of two silty sand layers sandwiched by a sand–gravel layer about 60 cm thick, which is covered by colluvial wedge and loess
W1/W2	Triangular red brown colluvial wedge (W1 and W2) near the fault, with sand and gravel mixed together
U4	Loess silty layer with an average thickness of about 3 m in the upper wall of the main fault covers the colluvial wedge W1
U5	Set of loess layers with relatively developed joints. The loess at its top contains more small gravel
U6	Light gray–brown loess with a few gravel and well jointed

TABLE 2 Summary of luminescence dating results from the Xujiabao profile on the LLSF.

Sample name	Depth (m)	Water (%)	Ra[a](Bq/kg)	Th[a](Bg/Kg)	K[a](Bg/Kg)	U[a] (Bg/Kg)	Da[b](Gy/ka)	De[c](Gy)	Age (ka)
XJB201704	2.50	1.51	31.7 ± 1.1	45.8 ± 1.52	555.2 ± 26.9	32.6 ± 7.9	3.2 ± 0.2	67.8 ± 2.6	21.2 ± 1.9
XJB201705	3.20	2.00	29.4 ± 1.0	41.6 ± 1.4	517.0 ± 25.0	48.3 ± 10.1	3.0 ± 0.2	78.8 ± 4.4	25.9 ± 2.6
XJB201710*	7.0	1	21.2 ± 0.4	31 ± 0.4	430.3 ± 8.0	38.5 ± 6.0	2.9 ± 0.1	119.4 ± 5.9	41.1 ± 2.4
XJB201713*	3.5	1	25.1 ± 0.5	34.3 ± 0.5	474.1 ± 8.9	39.8 ± 6.7	3.3 ± 0.1	95.7 ± 2.5	29.2 ± 1.2
XJB201722*	0.5	1	21.2 ± 0.5	39.7 ± 0.6	477.9 ± 10.1	22.6 ± 5.1	3.4 ± 0.1	11.3 ± 0.4	3.4 ± 0.2

[a]Uranium, thorium, and potassium concentrations were measured using an inductively coupled plasma mass spectrometer (ICP-MS).
[b]Da, annual dose.
[c]De, equivalent dose.
Note: XJB201704 and XJB201705 were prepared and analyzed by Key Laboratory of Crustal Dynamics, Institute of Crustal Dynamics, and CEA (Beijing, China), whereas XJB201710, XJB201713, and XJB201722 (marked by *) were analyzed by the State Key Laboratory of Earthquake Dynamics, Institute of Geology, and China Earthquake Administration (IGCEA) (Beijing, China).

understanding both the geodynamic mechanisms and strong earthquake hazard assessment of the SRS (Xu et al., 1992b, 1993; Xu and Ma, 1992).

The northern SRS lies at the northeastern corner of the Ordos Plateau, a piece of rigid continental lithosphere (Zhao et al., 2017). The seismicity in the northern SRS is of significant concern because it is adjacent to North China, one of the most densely populated regions on Earth. The cities of Beijing, Datong, Shijiazhuang, and Taiyuan, with a total population of more than 35 million people, all lie in or next to the northern Shanxi Rift system (Xu et al., 2002; Middleton et al., 2017; Rao et al., 2018).

The Liulengshan Fault is one of the major faults of the northern SRS, in which two moderate–strong earthquake swarms (Ms=6.1 and Ms=5.8) successively occurred in 1989 and 1991 (Wang and Wang,1992; Deng et al., 1994; Xu et al., 1996). Strangely, previous studies suggest that the Liulengshan Fault is dominated by normal faulting in the late-Quaternary and seems to have been slipping at a rate of 0.5 mm/a (Liu et al., 1991; Xu et al., 1996; Sun, 2018; Luo et al., 2022), but the focal mechanisms of the two moderate–strong earthquake are both strike–slip. The discrepancies between the focal mechanisms of the

moderate–strong earthquakes and the fault's sense from Quaternary geology are important for our understanding of how both crustal deformation and seismic hazard may vary through time. In addition, the previous work laid more emphasis on its geometrical structure and the fault slip rate. Because of human activity and intense erosion, the traces of the Liulengshan Fault are indistinguishable, and only Yin et al. (1997) carried out the paleoseismic research work, and the research on the paleoseismic activity history of the fault is weak at present.

To solve those problems, we mapped the fault traces using high-resolution satellite images and aerial photographs and conducted paleoseismic trench excavations at two sites along the Liulengshan Fault. Combined with the radiocarbon and optically stimulated luminescence (OSL) dating techniques, we worked out the paleoearthquake history in the late-Quaternary and analyzed the future seismic potential of this fault.

Geological background

The SRS varies in width from 20–80 km and is ~1,200 km long (Figure 1; State Seismological Bureau (SSB), 1988). The SRS
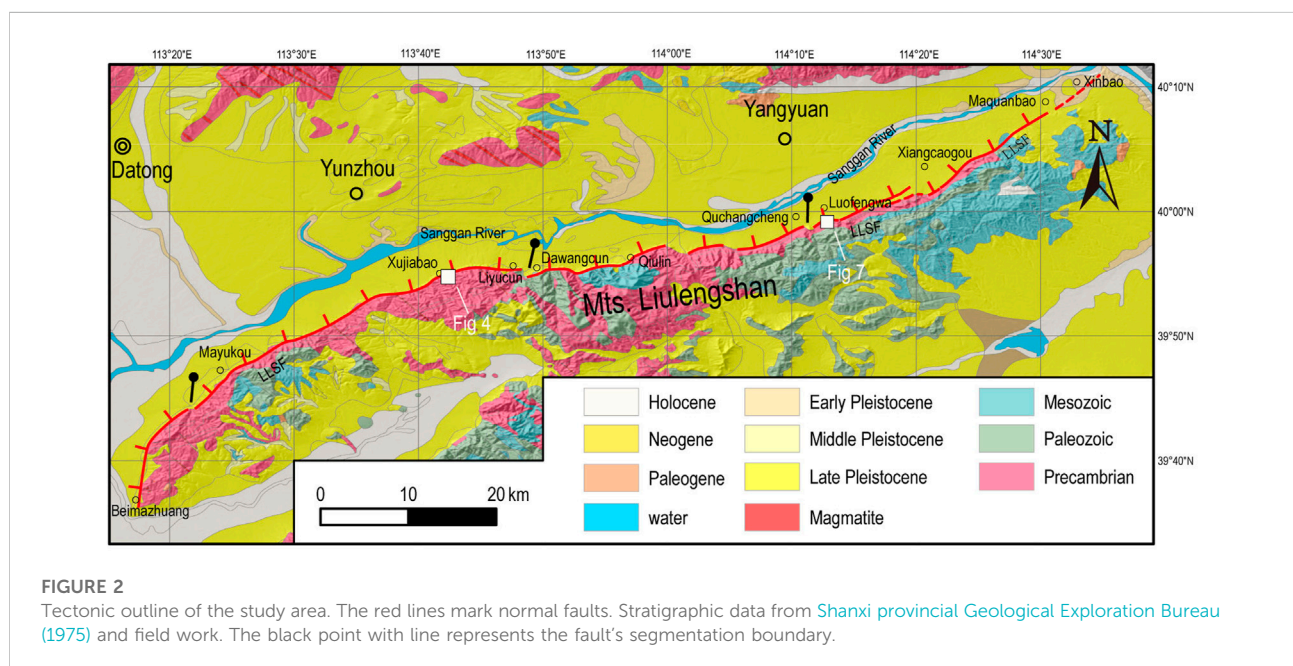
TABLE 3 Unit descriptions from the exposed walls of the Luofengwa trench.

Unit no.	Description
U1	The unit locates in the footwall side of the fault and has a total height of about 5 m. It can be divided into eight subunits based on the proportion, size, roundness, and other factors of the unit: u1-1 (the bottom), the gravel is 3–10 cm in diameter with medium roundness; u1-2–u1-5 (the middle), the diameter of the gravels which varies greatly, ranging from 5 to 40 cm, and the gravel with large diameter has better roundness, while the other gravel has medium roundness; u1-6–u1-8 (the top), the gravel content decreases and its roundness is medium, and the sandy clay content increases
U2	The unit locates at the bottom of the hanging side and can be divided into two subunits: u2-1 is the gravel layer, the gravel diameter is small, generally less than 2 cm, the roundness of which is good; the u2-2 is the red sand layer
U3	Red sandy clay layer about 1.5 m thick, of which u3-2 is the reddish brown ancient soil layer
U4	Reddish brown silty clay layer
U5	Reddish brown layer of silty soil with a small amount of fine gravel
W1	Triangular grayish brown wedges, with sand and gravel mixed together
W2	Reddish brown gravel silt, wedge shaped
W3	Gravel mixed packing wedge, gravel in all shapes and sizes, and poor roundness

is bound by north and northeast striking normal faults that form an S-shaped series of en echelon basins. These basins form a narrow, north–northeast-trending right-lateral transtensional zone in the middle sections and two wide, east–northeast-trending extensional segments marking its northern and southern terminations (Li et al., 1998; Yu, 2004; Luo et al., 2021). The initial extension in the SRS commenced at the end of the Miocene (Ye et al., 1987; Zhang et al., 1998, 2003), and the main phases of rifting occurred throughout the Shanxi Rift system during the Pliocene and Quaternary (State Seismological Bureau, 1988; Xu and Ma, 1992). It is likely that the location and geometry of the grabens are, in part, determined by preexisting, northeast striking, and fold-and-thrust belt

structures of the Late Triassic and Middle Jurassic-Cretaceous orogenies (Xu and Ma, 1992, 1993). Manifestations of these older orogenies are still evident today as a thickened crust (40–44 km) and a corresponding gravity anomaly over the region (Xu and Ma, 1992). Tapponnier and Molnar (1977) note that the width and length of individual grabens decrease from south to north, while the mean elevations of the graben floors increase (Li et al., 2015), suggesting a northward propagation of the onset of rifting through time.

The Liulengshan Fault runs along the northwestern side of the Liulengshan, an S-shaped mountain range in the center of the northern SRS, forming part of the eastern edge of the Datong Graben and the southern edge of the subsidiary Yangyuan Graben
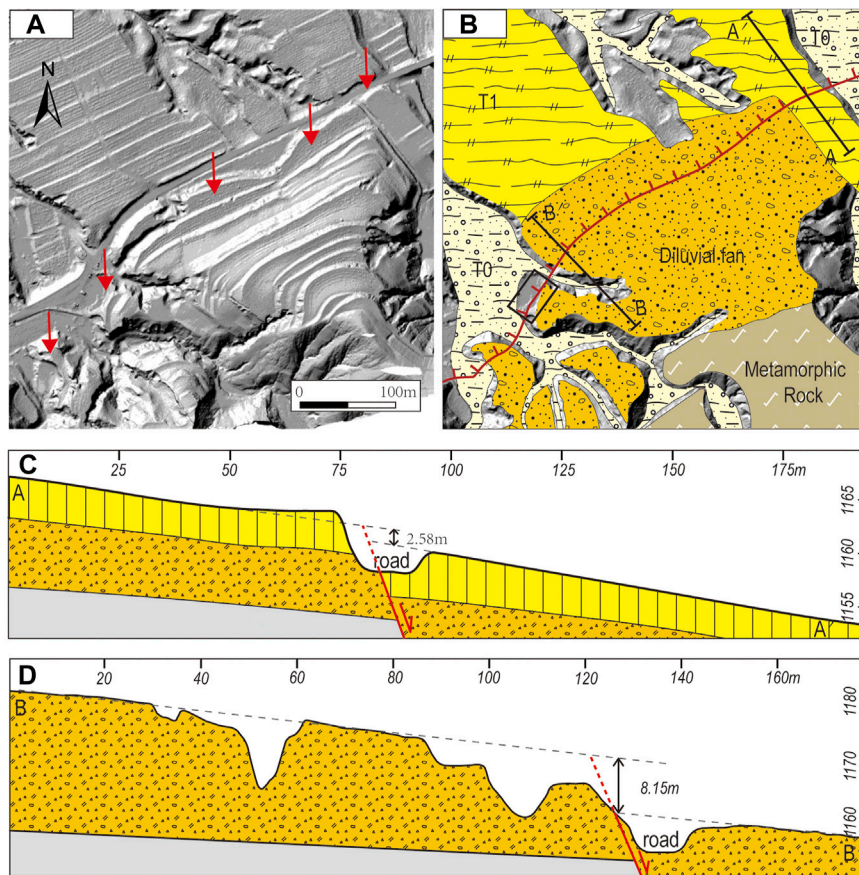

FIGURE 2
Tectonic outline of the study area. The red lines mark normal faults. Stratigraphic data from Shanxi provincial Geological Exploration Bureau (1975) and field work. The black point with line represents the fault's segmentation boundary.

FIGURE 3
Tectonic landforms and simplified stratigraphy profile near the Xujiabao trenching site. **(A)** s-UAV (small unmanned aerial vehicle) DEM imagery of the Xujiabao alluvial fan, where red arrows represent the trace of the Liulengshan Fault; **(B)** interpreted map. The red line indicates the trace of the Liulengshan Fault; T0–T1, alluvial phases; the black box in Figure 3B indicates the position of the trench; **(C)** and **(D)** as the topographic profiles for A–A′ and B–B′ in **(B)**, respectively. The color version of the figure is available only in the electronic edition.
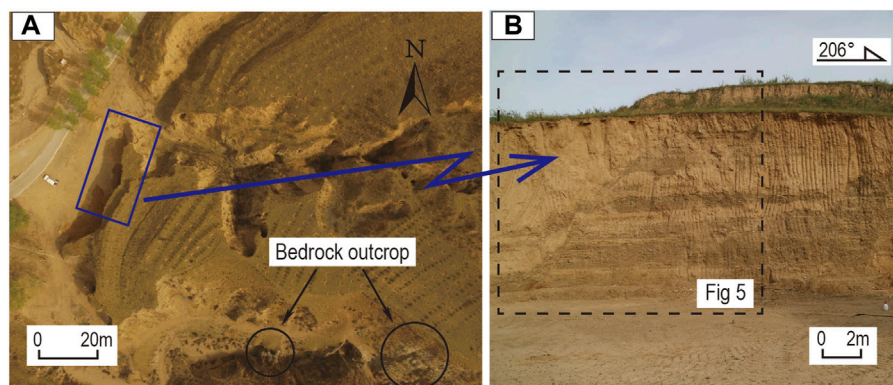
FIGURE 4
(A) Top view shows Site 1 near Xujiabao village. See Figure 1 for the location. **(B)** Field photograph of the fault zone.
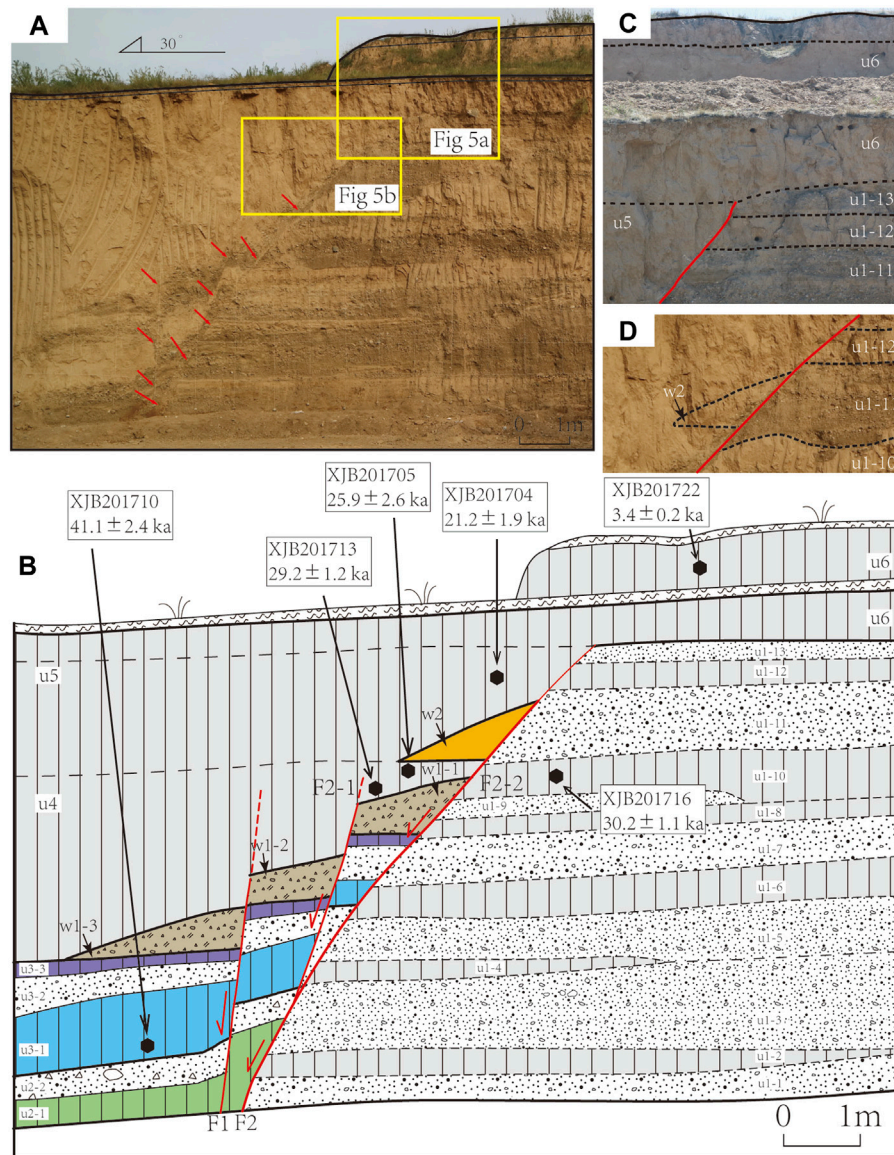
FIGURE 5
Photograph mosaic **(A)** and the interpreted map **(B)** of the Xujiabao profile. U denotes the stratum unit, and black lines show the stratigraphic contacts between units or subunits. Red lines show the fault planes. Small black filled hexagons show the locations of OSL samples, labeled with sample numbers and their ages (Table 2). **(C, D)**, Local enlarged photographs, showing the details of the trench exposures; see locations in **(A)**.

(Figure 2). The LLSF is a complex fault zone composed of a series of secondary faults. It starts from Xinbao of Yangyuan County in the east; passes Maquanbao, Luofengwa, Dawangcun, and Xujiabao in the west; and gradually transforms as the northeast-trending piedmont fault near Mayukou. It generally strikes east–northeast and dips north–northwest, for a total length of about 130 km. Based on previous geological and geomorphological investigations and studies of the geometric structure and segmentation of the fault, this study considers that the LLSF can be divided into four sections: Xinbao–Quchangcheng (XQ, 39 km), Quchangcheng–Dawangcun

(QD, 31 km), Dawangcun–Mayukou (DM, 34 km), and Mayukou–Beizhuang (MB, 27 km) (Deng et al., 1994; Duan and Fang, 1995; Cheng et al., 1996). There are inclined sequence discontinuities with a width greater than or equal to 1.5 km, which are generally covered by upper Pleistocene Malan loess, as fault boundaries between each section. The Xinbao–Quchangcheng section was active in the early Pleistocene, and the other three sections were active in the Late Pleistocene to Holocene (Xu et al., 1996).

The Liulengshan Fault has been active since the Late Pleistocene, with various displaced landforms, including linear
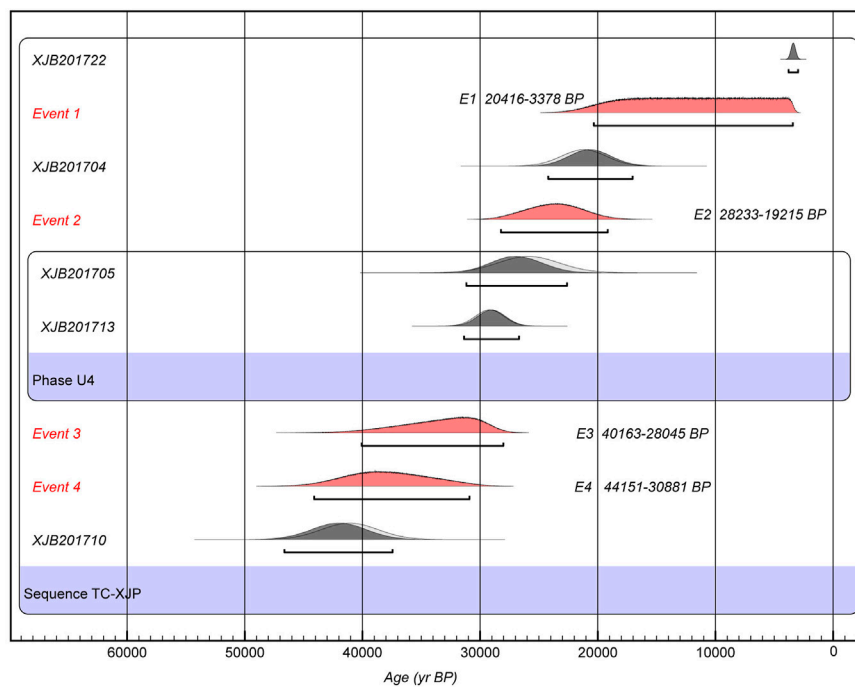
FIGURE 6
Results of OxCal analysis of luminescence dates from the Xujiabao trenching site. Unfilled areas are prior probability distributions, and solid curves are posterior distributions after OxCal analysis. Phases are summed probability for units with multiple luminescence dates.

fault scarps, bedrock fault surfaces, and offset streams. Based on detailed topographic measurements of typical displaced landforms, the vertical slip rates range from 0.2–0.6 mm/a, with an average value of 0.3 mm/a (Sun, 2018). Two earthquake swarms, with maximum magnitudes of Ms 6.1 and Ms 5.8, occurred on the Liulengshan Fault in October 1989 and March 1991, respectively (Xu et al., 2016). The focal depths of these earthquakes are thought to be in the range of 10–20 km (Xu et al., 1993) and there are no reports of surface ruptures associated with these events.
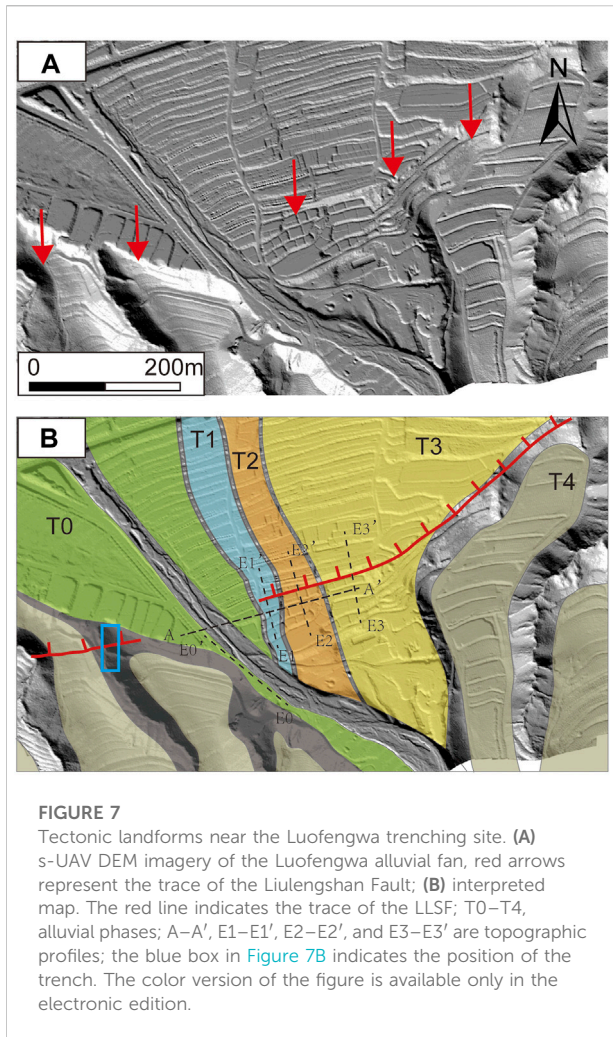
Study methods

Small unmanned aerial vehicle measurement

The study area is located in the north of Shanxi Province of China, a semi-arid area with sparse vegetation, most of which are low shrubs. We obtained the DEM (digital elevation model) and DOM (digital orthophoto map) data of the target area by using the s-UAV measurement (small unmanned aerial vehicle measurement). These data can truly reflect the topographic and geomorphological features and can provide assistance for identification of active faults

and their strike, as well as for the precise determination of parameters like displacement of the faults (James and Robson, 2012; Fonstad et al., 2013).

In this study, the DJI Phantom 3 unmanned aerial vehicle was used for image acquisition of the target area. The operating height of the aerial vehicle is 120 m, and the repetition rate of adjacent photos is up to 80%. The light intensity is relatively uniform throughout the whole process, without obvious shadow change. A total of 1,788 images in the RAW format have been collected. Agisoft PhotoScan, a semi-automatic software, was used for image processing. First, the images collected were stitched so as to reconstruct the point cloud data of the target area; second, the mesh grid model and orthophoto were generated. Finally, ground control points were added to generate the orthophoto with geographic coordinate information and the DEM (digital elevation model) (Verhoeven, 2011; Johnson et al., 2014; Wei et al., 2015).

Normal faults tend to form steep fault scarps and composite fault scarps, and these geomorphological phenomena can be clearly seen from the derived images (Figures 3,7). However, in some areas, fault scarps have been destroyed by human activities, which has a certain impact on extracting profile features from the images. In this article, two topographic profiles (Figures 3C,D) have been extracted from the area

FIGURE 7
Tectonic landforms near the Luofengwa trenching site. **(A)** s-UAV DEM imagery of the Luofengwa alluvial fan, red arrows represent the trace of the Liulengshan Fault; **(B)** interpreted map. The red line indicates the trace of the LLSF; T0−T4, alluvial phases; A−A′, E1−E1′, E2−E2′, and E3−E3′ are topographic profiles; the blue box in Figure 7B indicates the position of the trench. The color version of the figure is available only in the electronic edition.

near Xujiabao. The vertical displacements of the faults measured in the profiles are 2.58 and 8.15 m, respectively. Thus, the position of the faults has been determined from the geomorphology.

Trench excavation

Trenching is the most direct and efficient approach in paleoseismology to reveal evidence of faulting recorded in surface sediments. This method enables determining the paleoearthquake history of a fault (including the timing of earthquake occurrences, co-seismic displacement, and elapsed time) and understanding its rupture behavior, which is of great significance in accessing its seismic risk (Wallace, 1981; Sun et al., 2015; Liang et al., 2021). The key problem in the study of the paleoearthquake is the selection of the excavation site, which determines the success of its paleoseismic research. The selection of the location is based on the following two factors: whether we

can determine the period of earthquake events and whether enough samples are available for dating the events (Deng et al., 2004; Ran et al., 2012).

In front of the fault triangle or fault scarp, the channel becomes wider, and the waterpower weakens when it flows out of the mountains. In addition, the materials carried by the river would be accumulated and develop the alluvial–diluvial fan in the piedmont. The loess and alluvial–diluvial sediments with clear stratification since the Late Pleistocene epoch can not only record multiple seismic rupture events but also preserve enough sediment for dating, thus making it a relatively ideal environment for the study of paleoearthquakes.
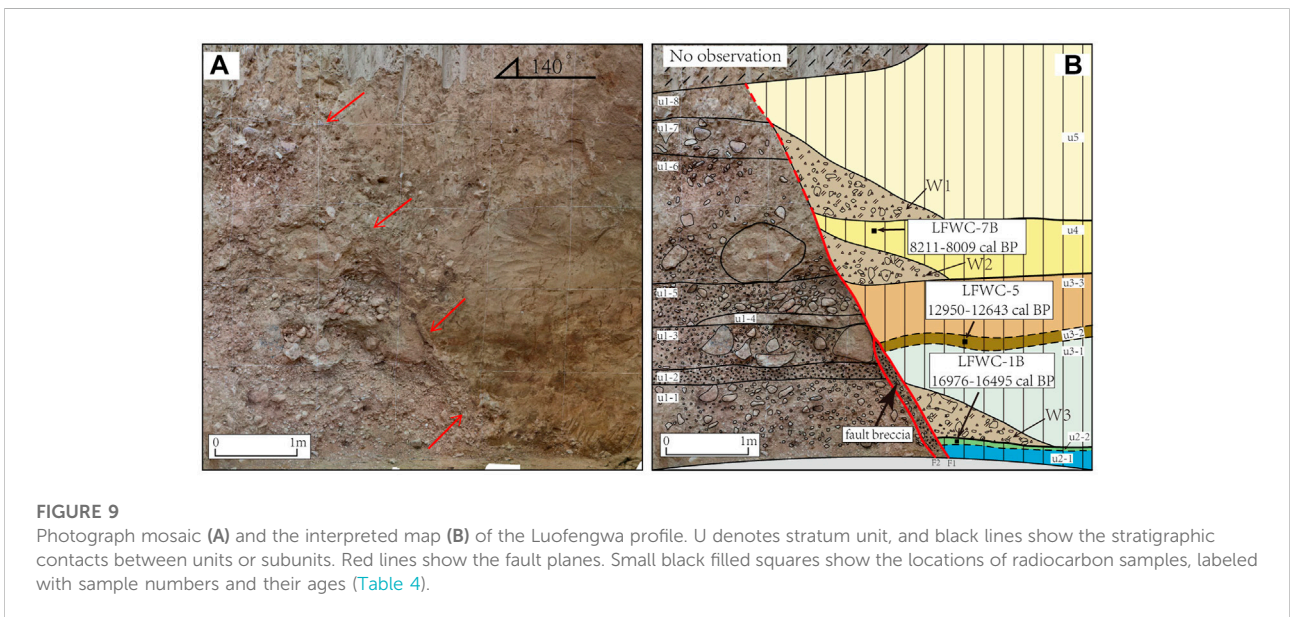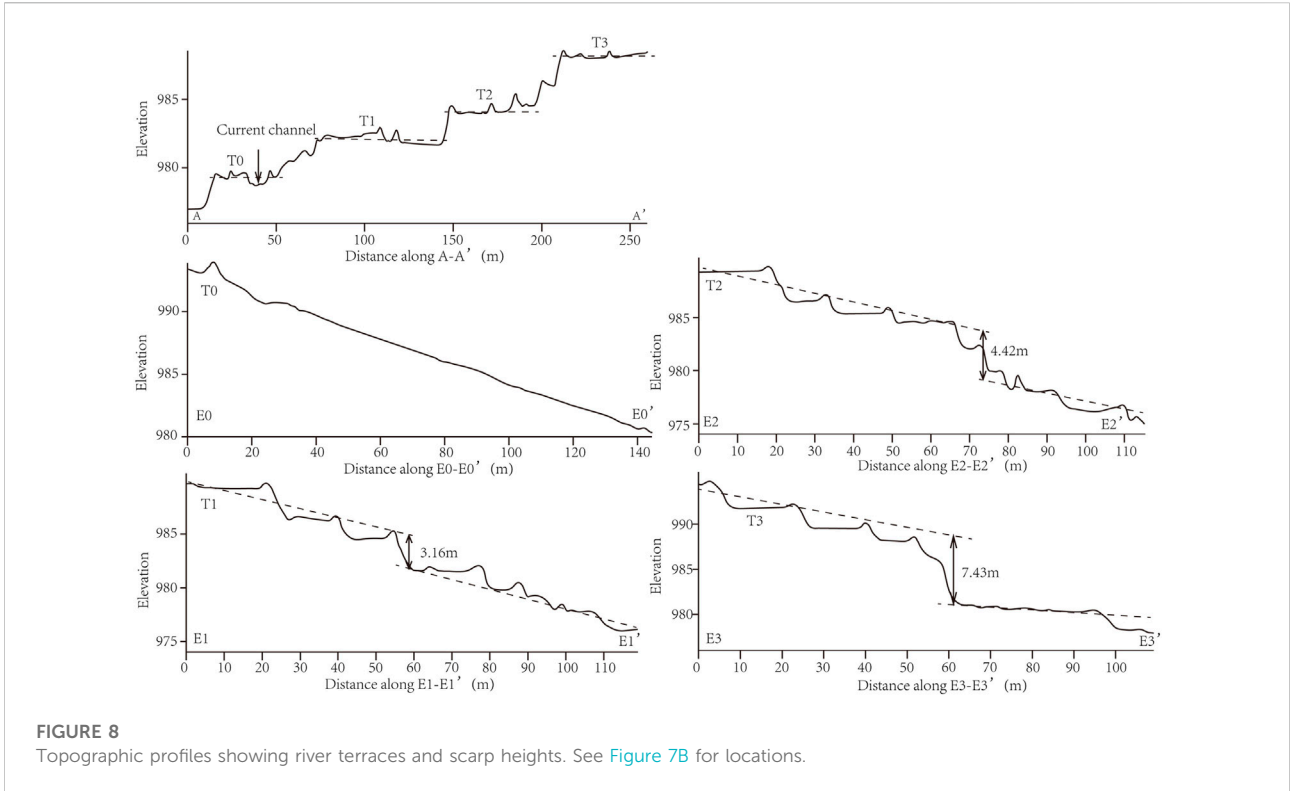
To confirm the location, geometry, and fault activity of the Liulengshan Fault, two trenches were chosen in Xujiabao and Luofengwa (for locations, see Figure 2). A single trench was excavated and described at each site, and strata were sampled for OSL dating. The details of the geomorphology, stratigraphy, and deformation of each site are described below.

Paleoseismic trenching

Xujiabao trench (39°54′59.65″N, 113°41′36.41″ E)

The Xujiabao trench is located in the central section of the LLSF, 25 km to the southwest of the Yangyuan County (Figure 2). At Xujiabao, the fault forms a prominent fault scarp that ranges in height from 2.5 to 8.5 m (Figure 3). The sediments to the north side of the LLSF are predominately fluvial deposits and alluvium covered by loess, and the sediments to the south side of the LLSF are predominately bedrock and pediments covered by thin strath terraces of alluvium and loess. This area is heavily modified by anthropogenic terracing of agricultural fields. We used optically stimulated luminescence (OSL) (Rapp and Aitken, 1998; Rhodes, 2011) to determine the age of the displaced buried sediments in the trenches. The samples were dated by the single-aliquot regeneration (SAR) method at the State Key Laboratory of Earthquake Dynamics (SKLED), Institute of Geology, China Earthquake Administration.

The trench at Xujiabao was excavated in the T1 terrace. The profile is about 8 m high and 12 m wide. It should be noted that the steep slope with a height of about half a meter left on the northeast side of the top of the profile due to removal of soil for road construction is not a fault slope but an artificial one (Figure 4). Six distinct lithologic units were identified in the trench walls and are described in detail in Table 1. The footwall is composed primarily of gravel on the southwestern side of the fault, overlain by U6 (Figure 5). The presence of gravel at the footwall has allowed accumulation of at least two distinct sediment wedges in the hanging wall. We have recognized three fault planes in the trench: faults F1 and F2-1 cut the lower units and terminates at the base of U5, and

FIGURE 8
Topographic profiles showing river terraces and scarp heights. See Figure 7B for locations.

FIGURE 9
Photograph mosaic **(A)** and the interpreted map **(B)** of the Luofengwa profile. U denotes stratum unit, and black lines show the stratigraphic contacts between units or subunits. Red lines show the fault planes. Small black filled squares show the locations of radiocarbon samples, labeled with sample numbers and their ages (Table 4).

fault F2-2 cuts the higher units and terminates at the base of U6.

On the trench wall, we recognized three fault strands (Figure 5), F1, F2-1, and F2-2. F2-2 and F2-1 sole into a single fault at depth, F2, that dips to the northeast and forms

the main tectonic contact between the hanging wall, with mainly loess sediments, and the footwall, with mainly sand and gravel sediments. The fault is present from the top to the bottom of the profile and controls the boundary of the colluvial wedge as the secondary order-faults of F2-1 and F1 have different activity

TABLE 4 Radiocarbon ages and calibrated dates for the samples from the Luofengwa trench.

Sample	Lab no[a]	Radiocarbon age (a BP)[b]	Calibration years (cal BP, 2σ uncertainties)[c]	Analyzed material[d]	Unit sampled
LFWC-1B	Beta-480767	13,830 ± 50	16,976–16495	Organic sediment	u2-2
LFWC-5	Beta-480770	10,850 ± 80	12,950–12643	Organic sediment	u3-2
LFWC-7B	Beta-480771	7,320 ± 50	8,211–8,009	Organic sediment	u4

[a]Samples were prepared and analyzed by the Beta Analytic Inc., United States.
[b]Using the accelerator mass spectrometry (AMS) method, the "conventional radiocarbon age" was calculated using the Libby half-life (5,568 years), which is corrected for total isotopic fraction and was used for calendar calibration where applicable. The age is rounded to the nearest 10 years and is reported as radiocarbon years before present (BP), "present" = AD 1950.
[c]Calibration was calculated by the IntCal 13 database (Reimer et al., 2013), with two standard deviation uncertainties and a confidence level of 95%.
[d]Types of samples collected for ^{14}C age dating.
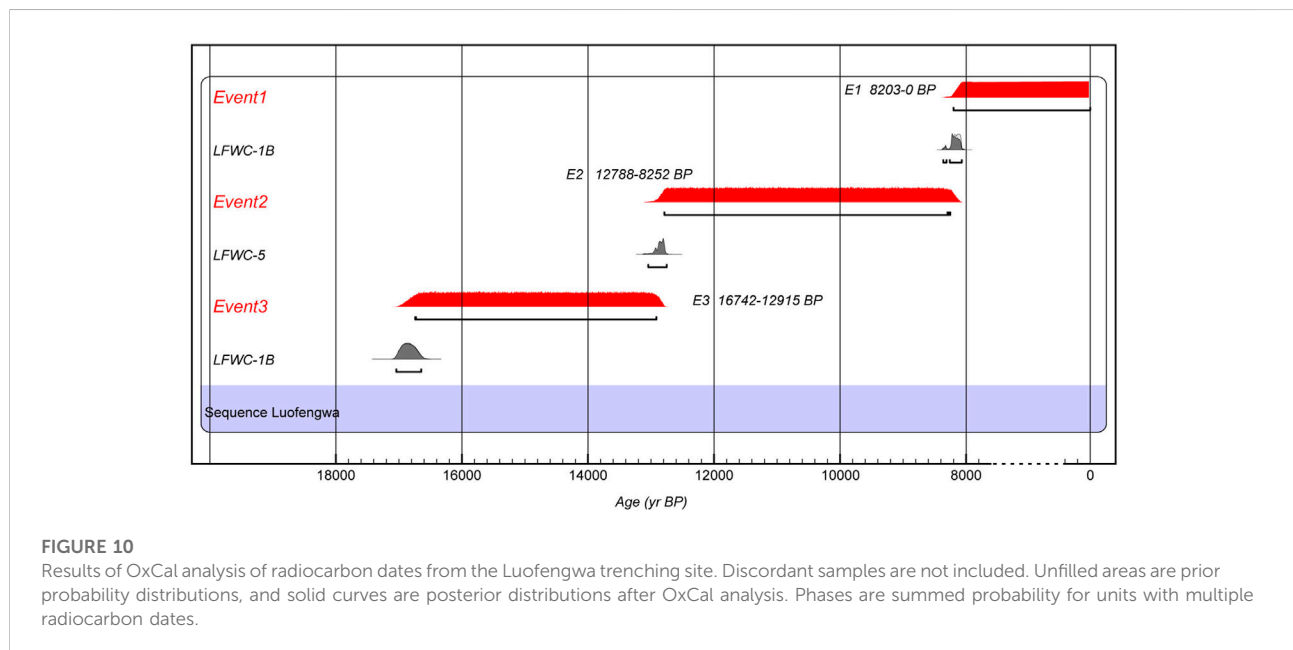
FIGURE 10
Results of OxCal analysis of radiocarbon dates from the Luofengwa trenching site. Discordant samples are not included. Unfilled areas are prior probability distributions, and solid curves are posterior distributions after OxCal analysis. Phases are summed probability for units with multiple radiocarbon dates.

stages and break different layers. The three faults are similar in geometry, dipping northeast. F1 and F2-1 are contemporaneous active faults, which fault u2 and u3 strata and colluvial wedge w1, with a vertical dislocation of about 1.2 m.

At least four paleoearthquake events can be identified in the profile, and we numbered E4–E1 for these events from old to new (Figure 6).

E4 event: after the deposition of u3-3, the main fault F2 (F2-2) was active, and all the strata below u3-3 were faulted. This event occurred between 41.1 ± 2.4 and 29.2 ± 1.2 ka, after which colluvial wedge W1 was accumulated and U4 was deposited.

E3 event: after the deposition of U4, the secondary faults F2-1 and F1 were simultaneously active and U4 and the colluvial wedge w1 accumulated in the E4 event were offset by this event and divided into w1-1, w1-2, and w1-3. Because the U4 stratum is mainly composed of a uniformly deposited loess silt layer, the colluvial wedge produced by this event is

difficult to recognize. This event also occurred between 41.1 ± 2.4 and 29.2 ± 1.2 ka.

E2 event: after the E3 event, the U4 stratum continues to deposit. The main fault F2 (F2-2) was active, and the colluvial wedge w2 was accumulated at the left of F2-2 after this event. Then, the U5 stratum was deposited. This event occurred at about or slightly before 21.2 ± 1.9 ka.

E1 event: because the colluvial wedge w2 and the bottom of U5 were offset, there was at least one event after E2, and the upper break point was not clear .

Luofengwa trench (39°59′02.17″N, 114°14′03.77″ E)

Luofengwa village is located in the southern margin of the Yangyuan Basin, adjacent to the LLSF. The fault cuts along the
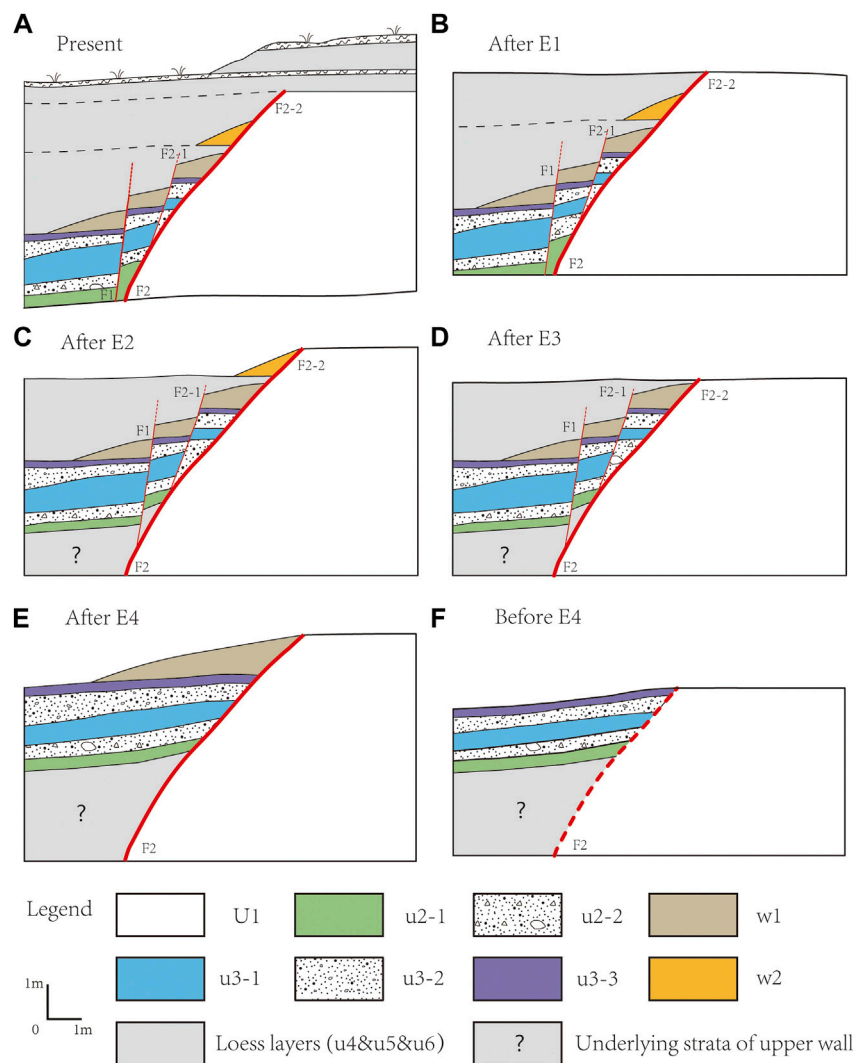
FIGURE 11
Possible restoration of the stratigraphy of the Xujiabao profile, showing the deformation associated with events E1 to E4. **(A)** Present-day situation; **(B)** colluvial wedge w2 and the bottom of U5 was offset, so there was at least one event after E2, and the upper break point was not clear; **(C)** E2 occurred after the deposition of U4 strata. The main fault F2 (F2-2) was active, and the colluvial wedge w2 was accumulated; **(D)** E3 occurred after the deposition of U4, the secondary fault F2-1 and F1 were simultaneously active, the U4 and the colluvial wedge w1 accumulated in the E4 event were offset by this event and divided into w1-1, w1-2, and w1-3; **(E)** E4 occurred after the deposition of u3-3, and the colluvial wedge W1 formed; and **(F)** possible original situation before E4.

back edge of a large alluvial fan south of Luofengwa village, cutting the Late Pleistocene to Holocene alluvial deposits within the basin, which strike 40–55°and dip ~75°NW (Deng et al., 1994; Xu et al., 1996).

About 1 km south of Luofengwa village, alluvial–diluvial fans are accumulated at the exit of the mountain and five terrace surfaces, namely, T0, T1, T2, T3, and T4 from low to high, were formed under the action of river erosion. The geomorphology of this section is well-preserved. Since the Late Pleistocene, the repetitive dislocation of faults has cut the geomorphic surface of different periods, and the height and vertical displacement of

fault scarps increase regularly with the periods of the geomorphic surface of faults. High-resolution measurement of the terrace profile shows (Figure 8) that terrace T0 maintains the original terrain slope, indicating that the fault has not been active since the terrace was formed. The latest faulting has dislocated T1 with a dislocation of 3.16 m. The dislocations of terrace T2 and T3 are 4.42 and 7.45 m, respectively.

The highest platform (T4) consists of loess capping sand and gravel. Near the fault, stream incision exposed an outcrop that reveals the lithology: the top is Malan loess, 3–5 m thick; the middle is gray–gray white gravel, silty sand, and gray–green clay
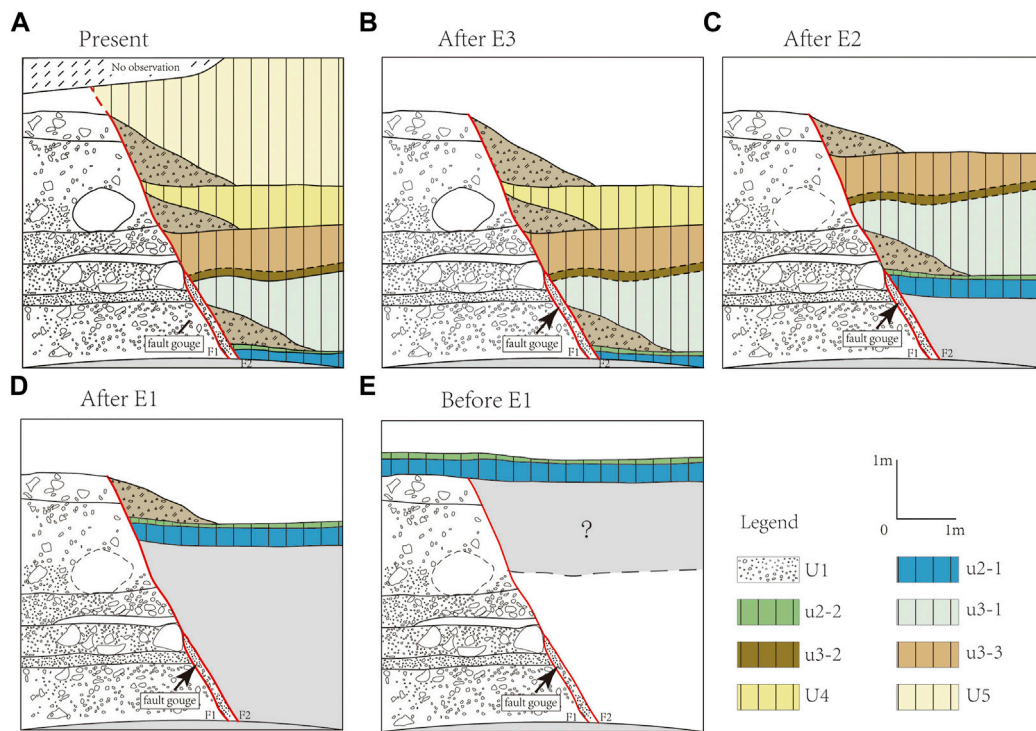
FIGURE 12
Possible restoration of the stratigraphy of the Luofengwa profile, showing the deformation associated with events E1 to E3. **(A)** Present-day situation; **(B)** E1 occurred after the deposition of u4, and colluvial wedge W1 formed; **(C)** E2 occurred after the deposition of u3-3, and colluvial wedge W2 formed; **(D)** E3 occurred after the deposition of u2-2, and colluvial wedge W3 formed; and **(E)** possible original situation before E3.
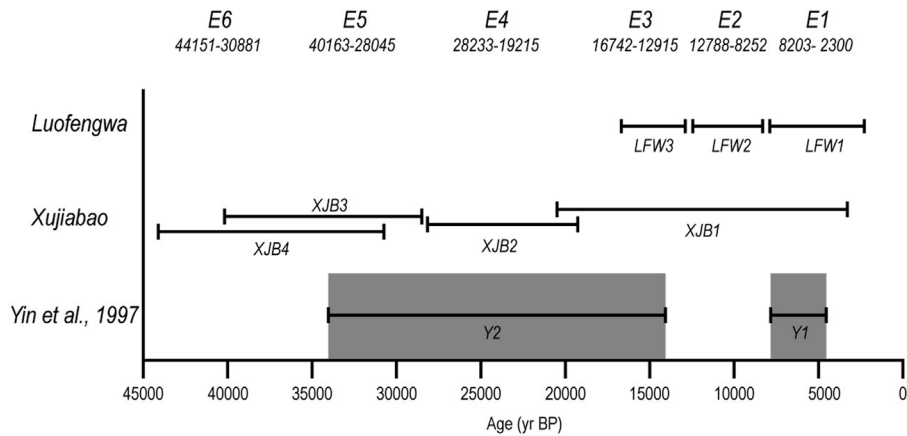

FIGURE 13
Late Pleistocene paleoearthquakes on the LLSF.

layer of the fluvio-lacustrine facies, which is about 12 m thick; and the bottom is metamorphic Proterozoic bedrock.

The excavated profile across the fault is about 5.5 m long and 5 m high. Figure 9 shows the overview photography and interpreted map of the stratigraphy exposed on the profile. The sediments on the two sides of the fault are different. The footwall mainly consists of alluvial gravels, and the hanging wall is mainly composed of sand and clay layers. The stratigraphy is

mainly divided into five units, wherein U1/U2/U3 are divided into several subunits, and they are numbered in ascending order from the bottom to the top (Figure 9). W1/W2 and W3 are identified as the colluvial wedges.

The description of each unit is summarized in Table 3.

On the trench wall, fault F1 cuts the sediments from the top to the bottom of the trench (Figure 9). Fault F2 is only present at the bottom of the profile. As the master fault, F1 dips to the northeast and forms a sharp boundary between the stratified Unit 1 and the overlying Units 2–5 that are exposed on the downthrown side.

Among various indicators for recognizing paleoearthquakes in unconsolidated sediments in a normal fault setting, the best and clearest evidence for fault rupturing of the ground surface includes the morphology of colluvial sediments (Burbank and Anderson, 2012). Based on the relation of the fault and colluvial wedges, at least three paleoearthquake events can be identified in the profile, and we numbered E1–E3 for these events from old to new (Figures 2–9).

In the trench, three samples for AMS-^{14}C dating have been collected and dated. Analyses were conducted at Beta Analytic Inc., United States, while detailed methods for sample preparation can be found at http://www.radiocarbon.com. Most of the result ages were calibrated using the INTCAL 04 database (Reimer, 2004). Calibrated radiocarbon ages are given in Table 4.

The E3 event occurred after the deposition of u2-2 and before u3-1, interpreting W3 as a colluvial wedge produced by the rupture. [14]C dating of the organic sediment from u2-2 and u3-2 gave the age of 16,976–16,495 and 12,950–12,643 years BP, respectively (Table 4). Therefore, the E3 event is constrained between 16,742–12,915 years BP, and we suggest that the age of the event is much closer to 12,915 years BP, as this was close to the ground surface prior to the deposition of the W3 wedge (Figures 9B,10; Table 4).

The E2 event occurred before U4 and after u3-3, again using the colluvial wedge of W2 as a key marker. U4 yields a ^{14}C age of 8,211–8,009 years BP (LFWC-7B; Table 4). Combining the age of u3-2, we constrained the E2 event to the period between 12,788 and 8,252 years BP, and we suggest that the age of the event is much closer to 8,252 years BP (Figures 9B,10; Table 4).

The E1 event is the youngest event in the trench and occurred before the deposition of u5 and after that of u4, using the colluvial wedge W1 that infilled a scarp produced by rupture along the fault. Accordingly, the E3 event that caused rupturing on this fault postdates the formation of u4, but a lack of datable material in the u5 means that the timing of this earthquake event cannot be accurately constrained. We are certain that the earthquake event occurred close to or slightly after ~8,203 years BP (Figures 9B,10; Table 4).

Discussion

Seismogenic capability of the Liulengshan Fault

Our paleoseismic analysis of the LLSF provides new evidence and more precise age constraints for the Late Pleistocene surface-faulting events. We determined four paleoseismic events in the Xujiabao trench, and five OSL samples with ages in correct stratigraphic order are used to constrain the events with very broad time ranges. On the Luofengwa trench wall, another three surface-rupturing events are correlated to colluvial wedges, and their timings are constrained by only three radiocarbon samples as organic materials were only found in the intervening sedimentary layers. Based on the lines of evidence, two restoration models of strata on trench walls are introduced to illustrate the seismic deformation and subsequent deposition in each trench (Figures 11, 12).

Yin et al. (1997) identified two events through trench excavations near our Luofengwa trench and determined their ages to be 14.2 ± 1.0–34.0 ± 2.2 ka and 4.6 ± 0.5–7.8 ± 0.6 ka based on IRSL dating (infrared stimulated luminescence). Among the events near Luofengwa, the age of the most recent paleoseismic event in the trench of Yin et al. (1997), Y1, overlaps with that of events LFW1 and XJB1, while the age of their older event overlaps with that of three paleoearthquakes XJB2, XJB3, and XJB4 in our trench. Yin et al. (1997) suggested that their latest event occurred around 6.7 ka. Therefore, we propose this event is the same paleoearthquake as our event E1. According to the overlaps of the ages of the events determined in the three trenches (Figure 13), we further determined six paleoearthquakes ruptured the LLSF with ages of 44,151–30,881, 40,163–28,045, 28,233–19,215, 16,742–12,915, 12,788–8,252, and 8,203–2,300 years BP.

The age of the latest paleoseismic event in the Xujiabao trench, event XJB1, is very wide (20,416–3,378 years BP) and coincides with the ages of all three paleoseismic events from Luofengwa, implying that they ruptured simultaneously during a single multi-segment rupture. Therefore, there are four possibilities for the faulting behavior of the LLSF: it either 1) ruptured each fault segment independently (independent 34 and 39 km ruptures), 2) ruptured between both trench sites (>50 km), 3) ruptured both two segments (34 + 39 km = 73 km), or 4) ruptured these two segments plus the additional two segments (130 km). Based on the empirical relationship between surface rupture length and moment magnitude for normal faults (Wells and Coppersmith, 1994; Blaser et al., 2010), these four rupture scenarios correspond to magnitudes Mw 6.9, 7.1, 7.3, and 7.7, respectively. Therefore, we suggest that the LLSF can generate an earthquake with a magnitude of 6.9–7.7.

Implications for seismic hazards

Due to the discontinuous stratigraphic deposition and poorly constrained ages of the determined paleoearthquakes, we cannot exactly tell the elapsed time of the most recent strong earthquakes on the LLSF. Datong, Shanxi Province, is the closest city to the fault and is about 30 km away. Datong was an important frontier county in ancient China and was built in the Warring States Period (about 300 BC), so it has a relatively complete historical record. Thus, information regarding damages caused by historic earthquakes was recorded very well since 300 BC in the near region. However, no strong earthquake was reported to happen on or near the LLSF in the Historical Strong Earthquake Catalog of China (China Earthquake Administration, 1999b). Therefore, we can estimate an elapsed time of >2,300 years since the latest strong earthquake. On the other hand, Deng et al. (1994) proposed a vertical slip rate of 0.4–0.8 mm/a through measuring and dating of several fault scarps, which were produced by multiple earthquake ruptures. According to the vertical slip rate and estimated elapsed time since the latest strong earthquake, the LLSF has accumulated an unreleased slip of 1.0–1.7 m, which is greater than the slip per event we observed in our trenches. That is to say, the LLSF has accumulated a seismic energy equivalent to moment magnitude of 6.8–7.0 according to the empirical relations between magnitude and slip for normal faults (Wells and Coppersmith, 1994). Therefore, we suggest there is a high seismic risk along the LLSF and in the nearby region.

Conclusion

Through two paleoseismological trenches at Xujiabao and Luofengwa, we revealed a ~42,000-year paleoearthquake history of the LLSF and confirmed that the fault has been active since the Late Quaternary and could produce surface-rupturing earthquakes. Based on the trench interpretations and the radiocarbon (C14) and optically stimulated luminescence (OSL) dating, we determined at least six surface-rupturing paleoearthquakes on the LLSF. The ages of these events, labeled E6–E1 from oldest to youngest, are limited to the following time ranges: 44,151–30881a, 40,163-28045a, 28,233-19215a, 16,742-12915a, 12,788-8252a , and 8203-2300a BP, respectively.

Compared with the previous results of Yin et al. (1997), we consider that different segments of the LLSF may rupture together at the same time. According to the empirical relationships between moment magnitude and rupture length, the best estimated magnitude is inferred to be in the range between Mw 6.9 and Mw 7.7. Considering the strong Late-Quaternary activity and a long earthquake elapsed time, we propose that the LLSF might have a high seismic hazard potential in the near future.

Data availability statement

The original contributions presented in the study are included in the article/Supplementary Material; further inquiries can be directed to the corresponding authors.

Author contributions

WS: conceptualization, methodology, and writing—original draft. HH: methodology, writing—review and editing, and funding acquisition. FS: conceptualization, field investigation, and writing—review and editing. HS: software and formal analysis. ZW: field investigation, and writing—review and editing. PS: field investigation and validation.

Funding

Acknowledgments

Conflict of interest

The author WS was employed by China Railway Engineering Design and Consulting Group Co., Ltd.

The remaining authors declare that the research was conducted in the absence of any commercial or financial relationships that could be construed as a potential conflict of interest.

Publisher's note

All claims expressed in this article are solely those of the authors and do not necessarily represent those of their affiliated organizations, or those of the publisher, the editors, and the reviewers. Any product that may be evaluated in this article, or claim that may be made by its manufacturer, is not guaranteed or endorsed by the publisher.

References

Blaser, L., Krüger, F., Ohrnberger, M., and Scherbaum, F. (2010). Scaling relations of earthquake source parameter estimates with special focus on subduction environment. *Bull. Seismol. Soc. Am.* 100 (6), 2914–2926. doi:10.1785/0120100111

Burbank, D. W., and Anderson, R. S. (2012). *Tectonic geomorphology (second edition) [M]*. Jersey City, United States: Wiley-Blackwell Publishing. doi:10.1002/9781444345063

Cheng, S. P., and Yang, G. Z. (1996). Late quaternary segmentation and segmented variations in tectonic geomorphology of southern marginal fault zone of Datong-Yangyuan basin. *Seismol. Geol.* 18 (4), 289–300.

China Earthquake Administration (1999a). *Historical strong earthquake catalog of China (2300 BC-1911 AD)*. Beijing: Earthquake Publishing House.

China Earthquake Administration (1999b). *Recent earthquake catalog of China (1912-1990, ms ≥ 4.7)*. Beijing: Chinese Sciences and Technology Press.

Deng, Q. D., Chen, L. C., and Ran, Y. (2004). Quantitative studies and applications of active tectonics. *Earth Sci. Front.* 11 (4), 383–392. doi:10.1007/BF02873097

Deng, Q. D., Nobuyuki, Y., Xu, X. W., and Suzuke, Y. (1994). Study on the late Quaternary kinematics of the northern piedmont fault of the Liulengshan Mountain. *Seismol. Geol.* 16 (4), 339–343.

Deng, Q. D., Ran, Y. K., Yang, X. P., and Min, W. (2007). *Map of active tectonics in China*. Beijing: Seismological Press.

Duan, R. T., and Fang, Z. J. (1995). Neotectonic characteristics of the northern piedmont fault of the Liuleng Mountain. *Seismol. Geol.* 17 (3), 207–213.

Ekström, G., Nettles, M., and Dziewonski, A. (2012). The global CMT project 2004–2010: Centroid-moment tensors for 13017 earthquakes. *Phys. Earth Planet. Interiors* 200-201, 1–9. doi:10.1016/j.pepi.2012.04.002

Fonstad, M. A., Dietrich, J. T., Courville, B. C., Jensen, J. L., and Carbonneau, P. E. (2013). Topographic structure from motion: A new development in photogrammetric measurement. *Earth Surf. Process. Landf.* 38, 421–430. doi:10.1002/esp.3366

James, M. R., and Robson, S. (2012). Straightforward reconstruction of 3D surfaces and topography with a camera: Accuracyand geoscience application [J]. *J. Geophys. Res.* 117 (F3), 1–17. doi:10.1029/2011JF002289

Johnson, K., Nissen, E., Saripalli, S., Arrowsmith, J. R., McGarey, P., Scharer, K., et al. (2014). Rapid mapping of ultrafine fault zone topography with structure from motion. *Geosphere* 1 0 (5), 969–986. doi:10.1130/ges01017.1

Lee, W. H. K., Wu, F. T., and Wang, S. C. (1978). A catalog of instrumentally determined earthquakes in China (magnitude ≥6) compiled from various sources. *Bull. Seismol. Soc. Am.* 68 (2), 383–398. doi:10.1785/bssa0680020383

Li, B., Atakan, K., Sørensen, M. B., and Havskov, J. (2015). Stress pattern of the Shanxi rift system, North China, inferred from the inversion of new focal mechanisms. *Geophys. J. Int.* 201 (2), 505–527. doi:10.1093/gji/ggv025

Li, Y., Yang, J., Xia, Z., and Mo, D. (1998). Tectonic geomorphology in the Shanxi graben system, northern China. *Geomorphology* 23, 77–89. doi:10.1016/s0169-555x(97)00092-5

Liang, K., He, Z., Ma, B., Tian, Q., and Liu, S. (2021). Joint-rupture pattern and newly generated structure of fault intersections on the northern margin of the Linhe Basin, northwestern Ordos Block, China. *Tectonics* 40, e2021TC006845. doi:10.1029/2021TC006845

Liu, G. X., Yu, S. E., Zhang, S. M., and Dou, S. Q. (1991). The north Wutaishan piedmont active fault zone in Shanxi. *Res. Act. Fault* 1, 118–130.

Liu, M., Cui, X., and Liu, F. (2004). Cenozoic rifting and volcanism in eastern China: A mantle dynamic link to the indo–asian collision? *Tectonophysics* 393 (1-4), 29–42. doi:10.1016/j.tecto.2004.07.029

Liu, M., Shen, Z., Wang, S., Wang, M., and Wang, Y. (2007). Active tectonics and intracontinental earthquakes in China: The kinematics and geodynamics. *Geol. Soc. Am.* 2425, 299–318. doi:10.1130/2007.2425(19)

Luo, Q. X., Li, C. Y., Li, X. N., Ren, G., and Dong, J. (2021). Slip distribution and footwall topography of the yanggao-tianzhen fault (northern Shanxi graben): Implications for the along -strike variations in fault activity and regional deformation. *Tectonics* 2021, e2020TC006593. doi:10.1029/2020tc006593

Luo, Q. X., Li, Y. L., Hu, X., Guo, A. L., Liu, Q. R., and Jiang, S. R. (2022). Constraints on the late quaternary dextral strike-slip rate of the Western segment of the north Liulengshan fault in the northern Shanxi graben system. *Quat. Sci.* 42 (3), 717–731. doi:10.11928/j.issn.1001-7410.2022.03.08

Middleton, T. A., Elliott, J. R., Rhodes, E. J., Sherlock, S., Walker, R. T., Wang, W., et al. (2017). Extension rates across the northern Shanxi Grabens, China, from

Quaternary geology, seismicity and geodesy. *Geophys. J. Int.* 209 (2), ggx031. doi:10.1093/gji/ggx031

Molnar, P., and Tapponnier, P. (1977). Relation of the tectonics of eastern China to the India-eurasia collision: Application of slip-line field theory to large-scale continental tectonics. *Geol.* 5, 212–216. doi:10.1130/0091-7613(1977)5<212:rottoe>2.0.co;2

Northrup, C. J., Royden, H., and Burchfiel, B. C. (1995). Motion of the Pacific plate relative to Eurasia and its potential relation to Cenozoic extension along the eastern margin of Eurasia. *Geol.* 23, 719–722. doi:10.1130/0091-7613(1995)023<0719:motppr>2.3.co;2

Ran, Y., Wang, H., Li, Y., and Chen, L. C. (2012). Key techniques and several cases analysis in paleoseismic studies in mainland China (1): Trenching sites, layouts and paleoseismic indicators on active strike-slip faults. *Seismol. Geol.* 34, 197–210. doi:10.3969/j.issn.0253-4967.2012.02.001

Rao, G., He, C. Q., Yu, Y. L., Hu, J. M., Chen, P., Yao, Q., et al. (2018). Active normal faulting along the langshan piedmont fault, north China: Implications for slip partitioning in the Western hetao graben. *J. Geol.* 126, 99–118. doi:10.1086/694748

Rapp, G., and Aitken, M. J. (1998). An introduction to optical dating: The dating of Quaternary sediments by the use of photon-stimulated luminescence. *J. Opt. Technol.* 68 (1), 2523–2528.

Reimer, P. J., Bard, E., Bayliss, A., Beck, J. W., Blackwell, P. G., Ramsey, C. B., et al. (2013). IntCal13 and Marine13 radiocarbon age calibration curves 0–50, 000 years cal BP. *Radiocarbon* 55 (4), 1869–1887. doi:10.2458/azu_js_rc.55.16947

Reimer, P. J. (2004). IntCal04: Terestrial radiocarbon age calibration, 0-26 cal kyr BP. *Radiocarbon* 46 (3), 1029–1058. doi:10.1017/S0033822200032999

Ren, J. Y., Tamaki, K., Li, S., and Zhang, J. (2002). Late Mesozoic and Cenozoic rifting and its dynamic setting in Eastern China and adjacent areas. *Tectonophysics* 344 (3-4), 175–205. doi:10.1016/S0040-1951(01)00271-2

Rhodes, E. J. (2011). Optically stimulated luminescence dating of sediments over the past 200, 000 years. *Annu. Rev. Earth Planet. Sci.* 39 (1), 461–488. doi:10.1146/annurev-earth-040610-133425

Shanxi Provincial Geological Exploration Bureau (SPGEB) (1975). *Scale of 1: 200,000 geological map of Datong*. Taiyuan.

Shen, Z., Zhao, C., Yin, A., Li, Y., Jackson, D. D., Fang, P., et al. (2000). Contemporary crustal deformation in East Asia constrained by Global Positioning System measurements. *J. Geophys. Res.* 105, 5721–5734. doi:10.1029/1999jb900391

State Seismological Bureau (SSB) (1988). *Research on active faults system around the Ordos block (in Chinese)*. Beijing: Seismological Press.

Sun, H. Y., He, H. L., Ikeda, Y., Kano, K., Shi, F., Gao, W., et al. (2015). Holocene paleoearthquake history on the Qingchuan fault in the northeastern segment of the Longmenshan Thrust Zone and its implications. *Tectonophysics* 660, 92–106. doi:10.1016/j.tecto.2015.08.022

Sun, W. (2018). *Late Quaternary activity of the northern Liuleng Mountain piedmont fault*. Beijing: Institute of Geology, China Earthquake Administration.

Tapponnier, P., and Molnar, P. (1977). Active faulting and tectonics in China. *J. Geophys. Res.* 82 (20), 2905–2930. doi:10.1029/jb082i020p02905

Verhoeven, G. (2011). Taking computer vision aloft: Archaeological three dimensional reconstructions from aerial photographs with photoscan [J]. *Archaeol. Prospect.* 18, 67–73. doi:10.1002/arp.399

Wallace, R. E. (1981). "Active faults, paleoseismology, and earthquake hazards in the Western United States," in *Earthquake prediction-an international review*. Editors D. W. Simpson and P. G. Richards (Maurice Ewing Series: American Geophysical Union), 209–216.

Wang, K., Ma, J., and Diao, G. (2012). Present-day stress state of the Shanxi tectonic belt. *Geodyn. Tectonophys.* 3 (3), 195–202. doi:10.5800/gt-2012-3-3-0071

Wang, L., Tian, Q., Li, D., and Zhang, X. (2011). The growth of the south margin fault of the Yuxian-Guangling basin in northwest Beijing area. *Seismol. Geol.* 33 (4), 828–838. doi:10.3969/j.issn.0253-4967.2011.04.008

Wang, M., and Wang, P. (1992). Focal mechanism and seismic tectonics of the 1989 Datong-Yanggao earthquake [J]. *Acta Seismol. Sin.* 6 (1), 59–69.

Wang, M., and Shen, Z. K. (2020). Present-day crustal deformation of continental China derived from GPS and its tectonic implications. *J. Geophys. Res. Solid Earth* 125, e2019JB018774. doi:10.1029/2019JB018774

Wei, Z. Y., Arrowsmith, R., He, H. L., and Guo, W. (2015). Accuracy analysis of terrain point cloud acquired by "structure from motion" using aerial photos [J]. *Seismol. Geol.* 37 (2), 636–648. doi:10.13140/RG.2.1.2282.3523

Wells, D. L., and Coppersmith, K. J. (1994). New empirical relationships among magnitude, rupture length, rupture width, rupture area, and surface displacement. *Bull. Seismol. Soc. Am.* 84 (4), 974–1002.

Wesnousky, S. G., Jones, L. M., Scholz, C. H., and Deng, Q. D. (1984). Historical seismicity and rates of crustal deformation along the margins of the Ordos block, north China. *Bull. Seismol. Soc. Am.* 74 (5), 1767–1783. doi:10.1785/BSSA0740051767

Working Group on Historical Earthquake Compilation of Shanxi Province Earthquake Administration (WGHECSPEA) (1991). *Compilation of historical earthquake literature in Shanxi Province*. Beijing: Seismological Publishing House, 476.

Xu, X. W., Han, Z. J., Yang, X. P., Zhang, S., Yu, G., Zhou, B., et al. (2016). *Seismotectonic map of China and its adjacent regions*. Beijing: Seismo-logical Press.

Xu, X. W., Ma, X. Y., and Deng, Q. D. (1993). Neotectonic activity along the Shanxi rift system, China. *Tectonophysics* 219, 305–325. doi:10.1016/0040-1951(93)90180-r

Xu, X. W., Ma, X. Y., and Deng, Q. D. (1992). Neotectonics of the Shanxi rift system, China. *Tectonophysics* 219, 40–53. doi:10.1016/0040-1951(93)90180-R

Xu, X. W., and Ma, X. Y. (1992). Geodynamics of the Shanxi rift system, China. *Tectonophysics* 208, 325–340. doi:10.1016/0040-1951(92)90353-8

Xu, X. W., Nobuyuki, Y., Suzuke, Y., and Deng, Q. D. (1996). Geomorphic study on late quaternary irregular faulting along the northern piedmont of Liulengshan range, Shanxi province, China. *Seismol. Geol.* 18 (2), 169–181.

Xu, X., Wu, W., and Zhang, X. (2002). *Latest crust movement and earthquakes in and around capital region*. Beijing: Science Press, 43–104.

Xu, Y. R., He, H. L., Deng, Q. D., Allen, M. B., Sun, H., and Bi, L. (2018). The CE 1303 Hongdong earthquake and the Huoshan piedmont fault, Shanxi Graben: Implications for magnitude limits of normal fault earthquakes. *J. Geophys. Res. Solid Earth* 123 (4), 3098–3121. doi:10.1002/2017JB014928

Ye, H., Zhang, B. T., and Ma, F. Y. (1987). The cenozoic tectonic evolution of the great north China: Two types of rifting and crustal necking in the great north China and their tectonic implications. *Tectonophysics* 133, 217–227. doi:10.1016/0040-1951(87)90265-4

Yin, G. M., Xu, X. W., Sun, Y. J., Chen, J., and Liu, A. G. (1997). Study on the paleoearthquake chronology of the Northern piedmont fault of the Liulengshan range of Yangyuan, Hebei province, China. *Earthq. Res. China* 13 (1), 18–26.

Yu, S. (2004). A study on characteristics of tectonic block motion and tectonic setting of strong earthquakes in northern part of the Shanxi fault depression zone. *Acta seimol. Sin.* 17 (4), 417–425. doi:10.1007/s11589-004-0021-5

Zhang, Y. G., Zheng, W. J., Wang, Y. J., Zhang, D. L., Tian, Y. T., Wang, M., et al. (2018). Contemporary deformation of the North China plain from global positioning system data. *Geophys. Res. Lett.* 45, 1851–1859. doi:10.1002/2017gl076599

Zhang, Y. Q., Ma, Y. S., Yang, N., Shi, W., and Dong, S. W. (2003). Cenozoic extensional stress evolution in North China. *J. Geodyn.* 36, 591–613. doi:10.1016/j.jog.2003.08.001

Zhang, Y. Q., Mercier, J. L., and Vergély, P. (1998). Extension in the graben systems around the Ordos (China), and its contribution to the extrusion tectonics of south China with respect to Gobi-Mongolia. *Tectonophysics* 285 (1-2), 41–75. doi:10.1016/S0040-1951(97)00170-4

Zhao, B., Zhang, C. H., Wang, D. Z., Huang, Y., Tan, K., Du, R. L., et al. (2017). Contemporary kinematics of the Ordos block, North China and its adjacent rift systems constrained by dense GPS observations. *J. Asian Earth Sci.* 135, 257–267. doi:10.1016/j.jseaes.2016.12.045